

Locally-refined free-surface flow simulations for moored and floating offshore platforms

Veldman, AEP; Luppens, R; van der Plas, P; van der Heiden, HJL; Seubers, H.; Duz, Bulent; Huijsmans, Rene; Helder, J.; Bunnik, T

Publication date

2016

Document Version

Final published version

Published in

Proceedings of the 26th International Ocean and Polar Engineering Conference

Citation (APA)

Veldman, AEP., Luppens, R., van der Plas, P., van der Heiden, HJL., Seubers, H., Duz, B., Huijsmans, R., Helder, J., & Bunnik, T. (2016). Locally-refined free-surface flow simulations for moored and floating offshore platforms. In A. M. Wang, J. S. Chung, T. Kokkins, & M. Muskulus (Eds.), *Proceedings of the 26th International Ocean and Polar Engineering Conference: ISOPE 2016* (pp. 83-90). Article ISOPE-I-16-504 International Society of Offshore and Polar Engineers (ISOPE).

Important note

To cite this publication, please use the final published version (if applicable).
Please check the document version above.

Copyright

Other than for strictly personal use, it is not permitted to download, forward or distribute the text or part of it, without the consent of the author(s) and/or copyright holder(s), unless the work is under an open content license such as Creative Commons.

Takedown policy

Please contact us and provide details if you believe this document breaches copyrights.
We will remove access to the work immediately and investigate your claim.

Locally-refined Free-surface Flow Simulations for Moored and Floating Offshore Platforms

Arthur E.P. Veldman¹, Roel Luppés¹, Peter van der Plas¹, Henri van der Heiden¹, Henk Seubers¹,
Bülent Düz^{2,3}, René Huijsmans², Joop Helder³, Tim Bunnik³

¹ Institute for Mathematics and Computer Science, University of Groningen, Groningen, The Netherlands

² Department of Ship Hydrodynamics, Delft University of Technology, Delft, The Netherlands

³ Maritime Research Institute MARIN, Wageningen, The Netherlands

ABSTRACT

The simulation of free-surface flow around moored or floating objects faces a series of challenges concerning the flow modelling and the numerical solution method. During the development of the ComFLOW simulation method many of these challenges have been tackled, as there are wave propagation, absorbing boundary conditions, turbulence modeling, fluid-solid body interaction and numerical efficiency. Several of these challenges will be discussed in the paper. To demonstrate the current capabilities of ComFLOW, a number of simulation results for engineering applications from the offshore industry will be presented. Examples are wave impact against a semi-submersible offshore platform, an oscillating buoy, and a free-fall life boat dropping into wavy water. For these applications, MARIN has carried out several validation experiments.

KEY WORDS: Extreme waves; fluid-solid body interaction; CFD; local grid refinement; experimental validation.

INTRODUCTION

Understanding the motion and behavior of the waves in nature has been a very popular subject among researchers from various fields of science. Nevertheless, even today when we have highly capable numerical methods and computational power at our disposal, particular aspects of numerical modeling of water wave propagation remain a formidable challenge. During the development of the ComFLOW simulation method (Kleefsman et al. 2005; Veldman et al. 2011) several of these challenges have been tackled:

a) To restrict the computational domain, waves should be allowed to freely enter or leave the domain. Thereto a new class of absorbing boundary conditions has been developed which is able to deal with the dispersive character of waves on deep water. I.e., their propagation speed is not known beforehand, but deduced from the local solution. We will discuss this issue below in more detail.

- b) Accurate wave propagation requires much attention to the description of the free surface. In particular its reconstruction and advection have to be carefully designed. More info is to be found in the PhD thesis of Düz (2015) and the forthcoming paper by Düz et al. (2016a).
- c) The turbulence model not only has to deal with the coarse grids that are common in engineering simulations, but should also recognize wall-bounded turbulence from free-surface turbulence. This will be tackled with a new class of adaptive, minimum-dissipation turbulence LES models; see e.g. Van der Heiden et al. (2015).
- d) The 'traditional' way of numerically coupling the flow dynamics with the dynamics of a floating object becomes unstable (or requires severe underrelaxation) when the added mass is larger than the mass of the object. To deal with this two-way interaction, a more simultaneous type of numerical coupling is being developed. This paper contains more details about this issue.
- e) The efficiency of the simulations is enhanced by means of local grid refinement and parallelisation.

Ad a). Typically, the phenomena of interest are local but embedded in a vast spatial domain, like the interaction between free-surface waves and man-made structures. For efficient computational modeling, this vast spatial domain around the region of interest is truncated via artificial boundaries, implying that a compact computational domain around the structure and a residual infinite domain are introduced; see e.g. papers on numerical wave tanks by Kim et al. (1999) and Koo and Kim (2004). A fundamental question surfaces: What is the boundary condition to be imposed on these artificial boundaries in such a way that the solution in the compact domain coincides with the solution in the original domain?

Here we enter the realm of absorbing or non-reflecting boundary conditions (ABC). Following the pioneering research by Engquist and Majda (1977), a wide variety of ABCs has been developed: nonlocal, semi-local or local operators, numerical dissipation zones and Dirichlet-to-Neumann (DtN) conditions. These conditions not only have to be considered from a theoretical modeling point of view

(well-posedness, modeling accuracy), but also from a numerical point of view (stability, numerical accuracy, efficiency). An impression of the work done thus far can be obtained from several review papers, like Givoli (1991), Tsynkov (1998), Hagstrom (1999), Appelö (2003) and Givoli (2004). For the work on ABCs done in the ComFLOW project we refer to the PhD theses of Wellens (2012) and Düz (2015). Below we will present our latest contributions to this issue which focus on the treatment of dispersive waves, i.e. waves whose propagation speed is not known beforehand but has to be deduced from the (local) solution.

Ad d). Another dimension to the above problem is added when the structures under study are not fixed in their position but free-floating or attached to a mooring system. Think for instance of moored offshore platforms (Johannessen et al. 2006), floating wind turbines (Bayati et al. 2015; Tran and Kim, 2015) or free-fall life boats (Tregde and Nestegard, 2013). Here the interaction between the incoming waves and the dynamics of the structure comes into play. Physically, we speak of one-way or two-way interaction. In the former case the structure ‘simply’ reacts to the oncoming flow field. But in the latter case the interaction is such that the motion of the structure influences the flow field around the structure. The latter case also poses most challenges to the numerical coupling between flow and structure.

A numerical coupling approach can be aggregated (monolithic) or segregated (partitioned, hierarchical). In the former case all discrete flow equations are combined into one single set of equations which is then solved simultaneously, i.e. as a whole. In the latter case two separate discrete systems (modules) can be recognized equipped with recipes to exchange information between the two separate modules. On the one hand this enhances the flexibility of the approach, but on the other hand it requires an iterative exchange of information between the modules with its (positive or negative) consequences for numerical stability and convergence. Below we describe our efforts to find a compromise between the robust monolithic approach and the more flexible but vulnerable partitioned approach. We will see that the ratio between the mass of the structure and its added fluid mass plays an essential role.

The organization of the paper is as follows. After an introduction of the flow equations, the absorbing boundary conditions are treated. Thereafter we present the numerical coupling strategy between fluid and solid structure. The paper presents a number of practical applications: an oscillating buoy, a falling life boat and a semi-submersible in waves; some of them are validated by experiments carried out at MARIN.



Fig. 1 Drop test with free-fall lifeboat (from: www.verhoef.eu)

MATHEMATICAL FLOW MODEL

The incompressible, turbulent fluid flow is modelled by means of the Navier–Stokes equations.

$$\mathcal{M}u = 0, \quad \frac{\partial u}{\partial t} + C(u)u + \mathcal{G}p - \mathcal{D}u = f. \quad (1)$$

Here \mathcal{M} is the divergence operator describing conservation of mass. Conservation of momentum is based on the convection operator $C(u)v \equiv \nabla(u \otimes v)$, the pressure gradient operator $\mathcal{G} = \nabla$, the diffusion operator $\mathcal{D}(u) \equiv \nabla \cdot \nu \nabla u$ and a forcing term f . The kinematic viscosity is denoted by ν . Turbulence is modelled by means of large-eddy simulation (LES) using a low-dissipation QR-model as described in Van der Heiden et al. (2015) and Veldman et al. (2015).

The Navier–Stokes equations (1) are discretized on a staggered Arakawa C-grid. The second-order finite-volume discretization of the continuity equation at the ‘new’ time level $^{(n+1)}$ is given by

$$M^0 u_h^{(n+1)} = -M^\Gamma u_h^{(n+1)}, \quad (2)$$

where M^0 acts on the interior of the domain and M^Γ acts on the boundaries. In the discretized momentum equation, convection $C(u_h)$ and diffusion D are discretized explicitly in time. The pressure gradient is discretized at the new time level. In this paper, for simplicity reasons the first-order forward Euler time integration will be used. In the actual calculations, the second-order Adams–Bashforth method is applied.

Taking the diagonal matrix Ω to denote the matrix containing the size of the control volumes, gives the discretized momentum equation as

$$\Omega \frac{u_h^{(n+1)} - u_h^{(n)}}{\delta t} = -C(u_h^{(n)}) u_h^{(n)} + D u_h^{(n)} - G p_h^{(n+1)} + f. \quad (3)$$

The discrete convection operator is skew-symmetric, such that convection does not contribute to energy production or dissipation; see Verstappen and Veldman (2003). In particular its discretization preserves the energy of the flow and does not produce artificial viscosity. To make the discretization fully energy-preserving, the discrete gradient operator and the divergence operator are each other’s negative transpose, i.e. $G = -M^{0T}$, thus mimicking the analytic symmetry $\nabla = -(\nabla \cdot)^T$. In this way, also the work done by the pressure vanishes discretely.

The solution of the discrete Navier–Stokes equations is split into two steps. Firstly, an auxiliary variable \tilde{u}_h is defined through

$$\Omega \frac{\tilde{u}_h - u_h^{(n)}}{\delta t} = -C(u_h^{(n)}) u_h^{(n)} + D u_h^{(n)} + f. \quad (4)$$

Secondly, imposing discrete mass conservation (2) on the new time level results in a discrete Poisson equation for the pressure:

$$\delta t M^0 \Omega^{-1} G p_h^{(n+1)} = M^0 \tilde{u}_h + M^\Gamma u_h^{(n+1)}. \quad (5)$$

The liquid region and the free liquid surface are described by an improved VOF-method; see Hirt and Nichols (1981) and Kleefsman et al. (2005).

ABSORBING BOUNDARY CONDITIONS

The derivation of a suitable ABC starts with a potential flow model for wave propagation. For waves of the form $\phi \sim e^{ik(x-ct)} \cosh(kz)$, at the free surface the dynamic and kinematic boundary conditions can be combined into a wave equation (shown for the two-dimensional case)

$$\frac{\partial^2 \phi}{\partial t^2} - c^2 \frac{\partial^2 \phi}{\partial x^2} = 0, \quad \text{where } c^2 \equiv \frac{g}{k} \tanh(kh) \quad (6)$$

is the dispersion relation relating the wave number k and the phase speed c . Left-running waves, like reflections at a right-hand side boundary, are suppressed by demanding

$$\frac{\partial}{\partial t} \phi + c \frac{\partial}{\partial x} \phi = 0. \quad (7)$$

This Smmerfeld (1949) condition has been proposed as a non-reflecting boundary condition by Engquist and Majda (1977). Higher-order versions can be formed by using powers of the left-hand side operator (Givoli, 2004).

Switching to the three-dimensional case, Higdon (1986, 1987) showed that it is possible to allow the wave under an angle of incidence α with the outflow boundary. In the higher-order conditions even more angles can be chosen: α_p , $p = 1, \dots, P$, where P is the order of the boundary condition. Higdon's condition reads:

$$\prod_{p=1}^P \left(\cos \alpha_p \frac{\partial}{\partial t} + c \frac{\partial}{\partial x} \right) \phi = 0. \quad (8)$$

To assess the benefit of using Eq. (8) as opposed to Eq. (7), we study the amount of spurious reflection as a function of the angle of incidence θ . For this purpose, at the artificial boundary the solution can be expressed as the sum of the outgoing and reflected waves

$$\phi(x, y, t) = e^{i(k_x x + k_y y - \omega t)} + R e^{i(-k_x x + k_y y - \omega t)}, \quad (9)$$

where the first term represents the wave with amplitude equal to unity impinging on the boundary, and the second term represents the spuriously reflected wave with amplitude R . To evaluate R , we substitute Eq. (9) into the general Higdon boundary conditions Eq. (8), and arrive at the following relation

$$|R_H| = \prod_{p=1}^P \left| \frac{\cos \alpha_p - \cos \theta}{\cos \alpha_p + \cos \theta} \right|, \quad (10)$$

where θ is the 'real' angle of incidence measured in the clockwise or counter-clockwise direction from the positive x -direction, $|\theta| < \pi/2$. It follows that Higdon's boundary condition (8) is non-reflecting as soon as θ equals one of the $\pm \alpha_p$'s, whereas (7) is non-reflecting for $\theta = 0$ only.

A comparison of the theoretical reflection coefficients for the various ABC variants is shown in Fig. 2.

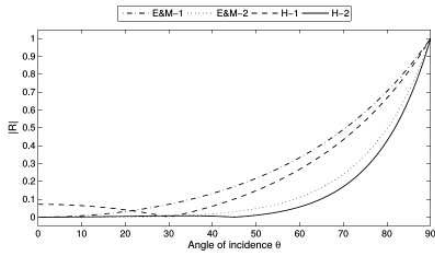


Fig. 2 Reflection coefficient of four absorbing boundary conditions versus the angle of incidence θ . E&M-1 and E&M-2 stand for the 1st- and 2nd-order Engquist-Majda ABC. The 1st- and 2nd-order Higdon ABC are denoted H-1 (with $\alpha_1 = 30^\circ$) and H-2 (with $\alpha_1 = 0^\circ$, $\alpha_2 = 45^\circ$), respectively.

In a Navier–Stokes context, the potential has to be related to the velocity (via the potential) and pressure (via the dynamic free-surface condition). Thus, it becomes a boundary condition featuring velocity and pressure, to be combined with the pressure Poisson equation (Düz, 2015).

Dispersive ABC

Because of the dispersion each individual wave component has its own phase speed c , hence a boundary condition like (8) cannot annihilate all these components. Is it possible to develop a boundary condition which

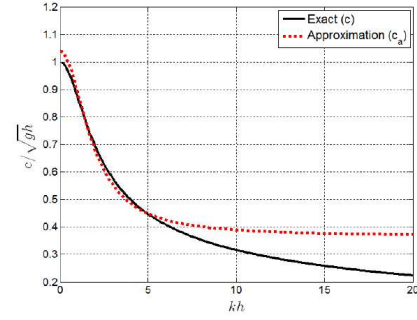


Fig. 3 Padé approximation of the dispersion relation. For the coefficients in (11), $a_0 = 1.04$, $a_1 = 0.106$ and $b_1 = 0.289$ are used.

allows a controlled amount of reflection for all these components?

Hereto, we introduce the following rational Padé expression which approximates the dispersion relation from (6) as

$$c_a = \sqrt{gh} \frac{a_0 + a_1(kh)^2}{1 + b_1(kh)^2}, \quad (11)$$

where a proper choice of coefficients a_0 , a_1 and b_1 leads to a close approximation for the targeted range of kh values. In Fig. 3 the difference between the two curves gives an indication for the amount of reflection caused by the rational approximation. A further improvement is introduced into the design of the boundary condition, by exploiting the exponential behavior of the wave potential in the z -direction. The wave number k is computed locally from the potential itself, via

$$k^2 \phi = \frac{\partial^2}{\partial z^2} \phi. \quad (12)$$

This relation can be substituted into (11) and combined with (8) to reach the final form of the 1st-order absorbing boundary condition ABC-1:

$$\cos \alpha \left(1 + b_1 h^2 \frac{\partial^2}{\partial z^2} \right) \frac{\partial \phi}{\partial t} + \sqrt{gh} \left(a_0 + a_1 h^2 \frac{\partial^2}{\partial z^2} \right) \frac{\partial \phi}{\partial x} = 0. \quad (13)$$

A stability analysis of this boundary condition can be found in the PhD thesis of Wellens (2012).

Dispersive Directional ABC

A further modification of the dispersive ABC will be discussed to account for both dispersive and directional effects of the waves. As the 2nd-order Higdon ABC has superior performance over the 1st-order one in terms of directional effects, we will incorporate the improvements that we made in the previous section by adding dispersive effects. As this ABC consists of the product of two operators, and considering the relations (11) and (12), we realize that only one of the operators can include the approximation for the dispersion relation. Otherwise, the product of two approximations would yield a fourth-order derivative in the z -direction which will cause difficulties when discretized at the boundaries. Therefore, we substitute the relations (11) and (12) in one of the operators. The resulting expression for the 2nd-order ABC-2 becomes

$$\left(\cos \alpha_1 \frac{\partial}{\partial t} + c \frac{\partial}{\partial x} \right) \left[\cos \alpha_2 \left(1 + b_1 h^2 \frac{\partial^2}{\partial z^2} \right) \frac{\partial \phi}{\partial t} + \sqrt{gh} \left(a_0 + a_1 h^2 \frac{\partial^2}{\partial z^2} \right) \frac{\partial \phi}{\partial x} \right] = 0. \quad (14)$$

An in-depth analysis of the implementation and effectiveness of these boundary conditions in practical situations can be found in the PhD thesis of Düz (2015) and the forthcoming publication Düz et al. (2016b).

Example

As an example of the use of the new type of absorbing boundary conditions we show some simulations of an oscillating sphere, with prescribed motion, producing a circular concentric wave pattern. The sphere with a radius of 4m is initially located 4m above the free surface and is allowed to make only vertical motion along the z -direction. Sinusoidal motion of the sphere is prescribed by $z_s(t) = 2 + 2 \cos(2.4t)$. After the impact of the sphere on the water surface initially at rest, a series of circular concentric waves is produced radiating outward from the center in all directions. To absorb these waves ABC-1 and ABC-2 are used at the outflow boundaries and their performance is compared.

A reference solution is obtained by repeating the simulation in a large domain: see Fig. 4 for the setup of the two domains. The length and the width of Ω_S is the same, $Lx_{\Omega_S} = Ly_{\Omega_S} = 50\text{m}$, and its depth is $Lz_{\Omega_S} = 10\text{m}$. Ω_L has the same depth but different length and width, $Lx_{\Omega_L} = Ly_{\Omega_L} = 400\text{m}$. The size of Ω_L is arranged in such a way that radiating circular waves do not reach the outflow boundaries of Ω_L throughout the simulation.

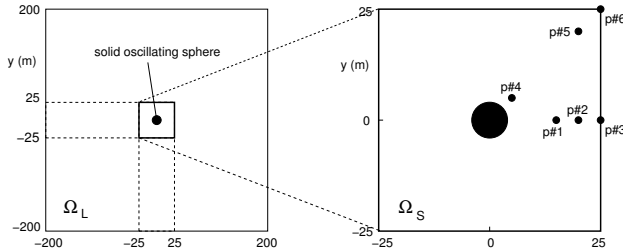


Fig. 4 Setup for the test with the oscillating solid sphere showing the domain sizes (left) and the positions of the wave probes (right). The solution in Ω_L is considered as the reference solution for the solution in Ω_S .

Two uniform grid resolutions of 0.25m and 0.5m are considered. Simulations are performed for 30s. The solution on the larger reference grid has been obtained with a grid size 0.25m. A large number of probes are placed in the domain to compare the free surface elevation records at various locations; see Fig. 4. Because of the prescribed motion of the sphere the generated circular wave is regular, and both the ABC-1 and ABC-2 are tuned to absorb this regular wave. However, since the wave is circular, it impinges on the outflow boundaries at different angles at different positions. To account for this directional effect, the angle coefficients in both boundary conditions are set to 45° .

Figure 5 shows the free surface elevation history from the first three probes on two grid resolutions. The results in the other three probes are comparable and can be found in Düz (2015). As the circular concentric wave travels out from the center, the amplitude of the wave decreases. This is due to the fact that the energy of the wave is spread over a larger area as the wave radiates from the center, which suggests that each particle of the wave gets less energy. This causes a decrease in the wave amplitude. The probes show a significant difference between the performance of the ABC-1 and ABC-2, and clearly demonstrate the superiority of the ABC-2 over ABC-1. The influence of grid refinement is much less, but does show the tendency of approaching the reference solution (but be aware that the latter has its own discretization error).

Figure 6 illustrates snapshots of the simulations at $t \approx 25\text{s}$ when ABC-1 and ABC-2 are used on the fine grid. With ABC-1 different amounts

of reflection at different locations result in a graphically-interesting but highly disturbed free surface. With ABC-2, however, the free surface is considerably less disturbed.

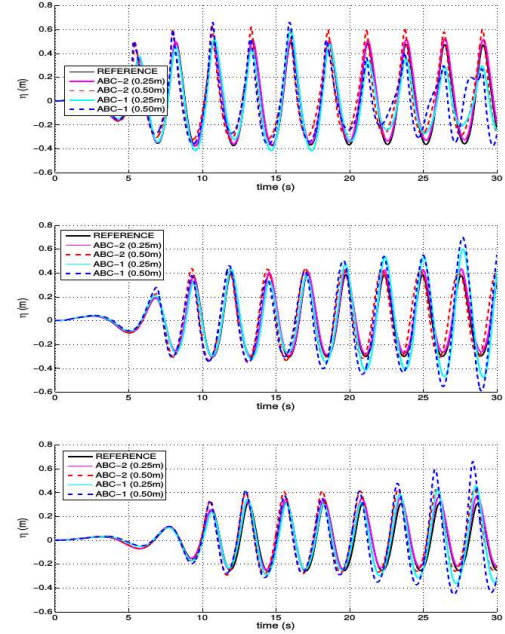


Fig. 5 Free surface elevations as a function of time at various locations for ABC-1 versus ABC-2 at two grid sizes. From top to bottom results are shown at p#1, p#2 and p#3.

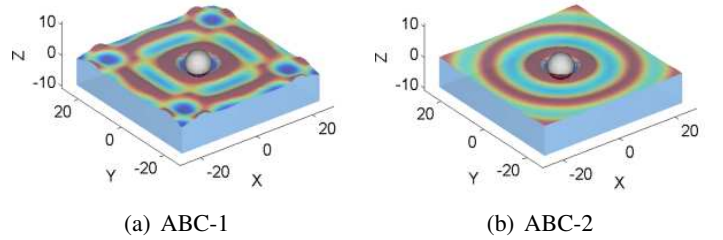


Fig. 6 Snapshots of the simulations of an oscillating sphere at $t \approx 25\text{s}$ (fine grid with resolution of 0.25m). The colors correspond with the vertical velocity at the free surface.

FLUID-SOLID BODY COUPLING

The next step is to allow the moving object to be freely floating or moored, when the fluid dynamics and the dynamics of the structure interact with each other. This physical two-way coupling has to be mirrored in the numerical coupling algorithm between the flow solver and the solid-body solver. Such a fluid-solid body system consists of three components. An example for each of them is given for a highly-simplified situation which we will later use to analyse the numerical stability of various coupling approaches. The three components are:

1. An equation describing the dynamics of the solid structure:

$$m_{\text{sb}} \ddot{x}_{\text{sb}} = f_{f \rightarrow s} + f_{\text{ext} \rightarrow s}, \quad (15)$$

where m_{sb} is the solid mass, x_{sb} its position, $f_{f \rightarrow s}$ the force exerted by the fluid on the solid, whereas $f_{\text{ext} \rightarrow s}$ is an external force (e.g. from mooring lines or due to gravity).

2. An equation describing the dynamics of the fluid:

$$m_{ad}\ddot{x}_{fl} = f_{s \rightarrow f} + f_{ext-f}, \quad (16)$$

where x_{fl} describes the motion of the boundary of the fluid domain, whereas the resistance $f_{s \rightarrow f}$ of the fluid to the acceleration \ddot{x}_{fl} defines the added mass m_{ad} . Again, f_{ext-f} is an external force field (e.g. due to gravity).

3. Equations relating the solid-body problem to the fluid flow problem, in particular an exchange of the position of the solid body and of the mutual force fields:

$$\text{position } x_{sb} = x_{fl}; \quad \text{force } f_{s \rightarrow f} = -f_{f \rightarrow s}. \quad (17)$$

Numerical Coupling

The coupling of these components can be done in an *aggregated/monolithic* or *segregated/partioned* way. A monolithic coupling removes the numerical solution procedure from each individual component, and recombines them into one single global solver. This is numerically advantageous, since information from all components is available simultaneously. However, software architecture has to allow this, and it may be hard to profit from the specialized individual solution procedures. In the model problem, (17) can be used to eliminate the unknown forces from (15) and (16), after which we obtain one ‘single’ monolithic equation

$$(m_{sb} + m_{ad})\ddot{x} = f_{ext-s} + f_{ext-f}. \quad (18)$$

Alternatively, a partioned coupling retains the existing model infrastructure, and adds a layer of communication between the components, cf. (17). This layer acts as a boundary condition to each component, carrying over information between the components. As such, the layer imposes a direction on the flow of information over the connections, altering the numerical properties of the system. Built on top of the communication layer, the global solver only solves for the boundary/interface conditions. For the above model problem this would look like

$$\text{solid } m_{sb}\ddot{x} = f + f_{ext-s}, \quad \text{fluid } m_{ad}\ddot{x} = -f + f_{ext-f} \quad (19)$$

where the subscripts can be omitted because of (17).

In case of time-dependent problems, the additional flexibility in the time-discretization of these boundary conditions allows them to be arranged for an *explicit* or *implicit* coupling procedure. An explicit procedure extrapolates the boundary conditions from the past, such that the global solver is no more than a single evaluation of each of the components. The extrapolation necessarily introduces a time lag which alters and often destabilizes the system. An implicit procedure on the other hand interpolates the boundary conditions from repeated evaluation of all components, converging to a fixed point. Upon convergence, the time lag effect is avoided, at the cost of extra computational work.

Because of its flexibility, the segregated, partitioned approach will be adopted in this work. Then we will have to define in which order information is exchanged between the two subsystems. An intuitive way is to prescribe the force exerted by the fluid to the object and in return pass the new body location to the fluid. This way of information exchange is called a weak coupling method. For the model problem it looks like:

$$\text{solid } m_{sb}\ddot{x}^{(old)} = f^{(old)} + f_{ext-s}, \quad \text{fluid } f^{(new)} = -m_{ad}\ddot{x}^{(old)} + f_{ext-f}. \quad (20)$$

Its convergence is governed by the iterative process

$$f^{(new)} = -\frac{m_{ad}}{m_{sb}} f^{(old)}. \quad (21)$$

This process clearly diverges when $m_{ad}/m_{sb} > 1$, i.e. when the added mass m_{ad} is larger than the solid body mass m_{sb} . It can be stabilized, but at the cost of severe underrelaxation and correspondingly large computational effort.

In a time-dependent problem, during each time step a similar iterative procedure has to be followed. In FSI terminology, this is called subiteration. When the added mass is large, typically dozens of subiterations (subcycles) per time step have to be carried out. In each of them a pressure Poisson equation has to be solved, making the calculations expensive.

Quasi-Simultaneous Coupling

The monolithic approach (18) involves no subiterations, so we would like to get as close as possible to that approach. That can be achieved when a simple approximation of the (usually complicated) solid-body dynamics is available. In an aerodynamical context this approximation is called *interaction law* (Veldman, 1981). Nowadays, in modern domain-decomposition terminology, it would be called an approximate Dirichlet-to-Neumann operator. It should be so simple that it can easily be included in the fluid-flow solver and solved simultaneously with the flow equations; yet, it has to contain sufficient information of the ‘real’ model. Thus this approach has been called *quasi-simultaneous* (Veldman 1981, 2001, 2009); see Fig.7.

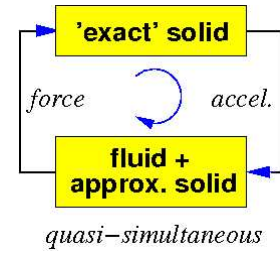


Fig. 7 The quasi-simultaneous coupling method

The interaction law basically anticipates how the solid body reacts to changes in the forces exerted by the fluid. Thus it is formulated as an approximate (local) quasi-linearization to the solid body model (20a):

$$m_{qs}(\ddot{x}^{(new)} - \ddot{x}^{(old)}) = f^{(new)} - f^{(old)} \quad \text{with} \quad m_{sb}\ddot{x}^{(old)} = f^{(old)}, \quad (22)$$

where m_{qs} approximates the Jacobian of the solid body dynamics; in our simplified case it approximates m_{sb} . Note that in general the latter represents the full physics of the solid body dynamics, including mooring lines etc.; m_{qs} can be much simpler. The interaction law (22) is combined with the fluid flow model (20b) at the new iteration level.

Re-arranged, the quasi-simultaneous method reads

$$\text{solid body } m_{sb}\ddot{x}^{(old)} = f^{(old)} + f_{ext-s} \quad (23)$$

$$\text{fluid } \begin{cases} m_{qs}\ddot{x}^* - f^{(new)} = m_{qs}\ddot{x}^{(old)} - f^{(old)} \\ m_{ad}\ddot{x}^* + f^{(new)} = -f_{ext-f} \end{cases} \quad (24)$$

where the superscript $*$ denotes that this quantity is not being used in the further iterations. The equations in the fluid (24) are solved simultaneously, using (23) to eliminate $\ddot{x}^{(old)}$, to yield

$$\left(\frac{1}{m_{ad}} + \frac{1}{m_{qs}}\right) f^{(new)} = \left(\frac{1}{m_{qs}} - \frac{1}{m_{sb}}\right) f^{(old)} - \frac{f_{ext-s}}{m_{sb}} - \frac{f_{ext-f}}{m_{ad}}. \quad (25)$$

For $m_{qs} = \infty$ the weak coupling method (21) is recovered, with its amplification factor $-m_{ad}/m_{sb}$. The optimum would be to select $m_{qs} = m_{sb}$, as

then the monolithic method (18) is recovered which does not need to iterate at all. But any choice close to m_{sb} will do, as the quasi-simultaneous method converges (without underrelaxation) if and only if

$$\frac{1}{m_{qs}} > \frac{1}{2} \left(\frac{1}{m_{sb}} - \frac{1}{m_{ad}} \right). \quad (26)$$

When $m_{ad} > m_{sb}$, i.e. when the weak coupling diverges, a maximum exists on the allowable m_{qs} , but in all cases $0 < m_{qs} < 2m_{sb}$ is safe.

The above exposition has been kept sketchy to bring out its essentials better. In applications with fluid flow, the m_{ad} symbolizes the solution of the Navier–Stokes equations, and details of the quasi-simultaneous coupling become much more technical. A verbal description: In each fluid point at the body surface, the interaction law, relating the pressure p acting on the solid body to the displacement of the body (governed by u), is used as a boundary condition to the flow equations. In particular, it is applied to the pressure Poisson equation (5). In this way, the fluid flow is immediately anticipating of the reaction of the solid body.

Example

As an example, we present simulations of a life boat falling into a breaking, extreme wave. A snapshot of the simulations is shown in Fig. 8. The dynamics of the life boat is modelled with a 6-DOF mechanical model.

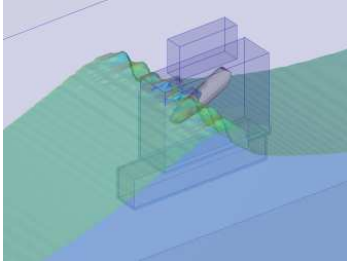


Fig. 8 A snapshot of the life boat falling into a large wave. Also the locally-refined grid regions are shown.

The fluid flow is modelled with the Navier–Stokes equations and solved on a grid consisting of about 0.7 million active (i.e. within the fluid) grid points, with local grid refinement around the life boat (Fig. 8); see Van der Plas et al. (2015). For physical accuracy this grid is rather coarse, but the focus in these simulations is on the numerical behaviour of the coupling process. Thus both the weak coupling procedure (21) as well as the quasi-simultaneous procedure (24) have been applied. In the latter case, the interaction law is based on the under-water part of the life boat (as the Poisson equation is only solved under water).

The most important result concerns the amount of work that is needed per time step to achieve the coupling between solid-body dynamics and fluid flow. The weak method often requires dozens of subcycles, in each of which a Poisson equation has to be solved. This number is dependent on the amount of fluid that is moved aside by the moving body, represented by the added mass m_{ad} . Fortunately, the later subiterations have a good initial guess so they are not as expensive as the earlier ones. Thus the amount of work is better represented by the total number of SOR-iterations (Botta and Ellenbroek, 1985) needed for all Poisson solves within one time step; this amount of work is shown in Fig. 9. The relation with the added mass becomes visible when plotting the time history of the estimated added mass in Fig. 9. Comparison with Fig. 9 shows a clear correlation between the number of iterations and the mass ratio m_{ad}/m_{sb} . In contrast, the quasi-simultaneous method requires 1 or 2 subiterations,

resulting in much less work per time step (Fig. 9). We remark that the ‘gap’ in the added-mass estimation (around $t = 4$ sec) occurs because the latter becomes numerically highly inaccurate (loss of figures).

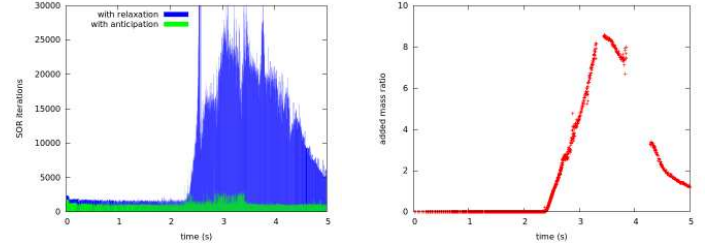


Fig. 9 *Left*: The number of SOR iterations per time step for the underrelaxed weak coupling method (blue) and the anticipating quasi-simultaneous method (green). *Right*: The estimated added mass for the falling lifeboat as a function of time (the gap around $t = 4$ is due to loss of figures). Note the resemblance between both graphs.

WAVE IMPACT

In a final example we present simulations and experiments for run-up against a (fixed) semi-submersible offshore platform. Model experiments have been carried out at MARIN to provide validation material; the setup of the experiments is sketched in Fig. 10. They are carried out on a scale of 1 : 50. A simplified semi-submersible is located in the center of the flow domain. On full scale it measures 114.5 m \times 17.5 m \times 28.0 m with a draft of 16.0 m. The waves in the experiment are generated by a flap-type wave generator. The basin width is 4 m, i.e. 200 m on full scale, with solid side walls. The incoming wave has a full scale wave height of 14.7 m and a wave period of 11.0 s. The wave elevation and pressure are measured at several positions, indicated in Fig. 10.

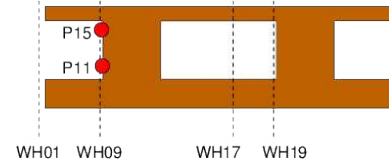


Fig. 10 Wave run-up against a semi-submersible: snapshot of experiment (top) and position of sensors (bottom).

To reduce computational costs, the boundaries of the flow domain are brought closer to the structure than in the experiment. Its inflow boundary is located at 240 m from the center of the semi-submersible. To facilitate this decreased distance between the wave maker and the semi-submersible in the simulations, the incoming waves have been analyzed by wave calibration tests (without semi-submersible in

the flow) to establish a representative incoming computational wave (Iwanowski et al. 2009). The generated incoming wave is modeled as a 5th-order Stokes wave. Note that the shape of the experimental wave differs from a theoretical Stokes wave: the wave crests can be made to correspond nicely, but a difference in the troughs is left. This has to be taken into account when comparing the simulations with the model tests.

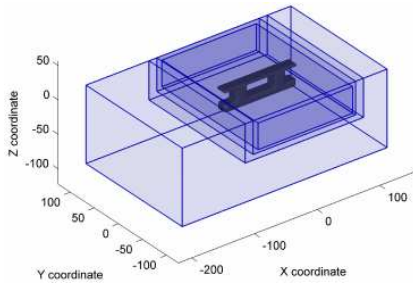


Fig. 11 The grid with local refinements around the free surface and around the semi-submersible. Each box contains a refined grid level (no grid lines are shown).

The ComFLOW simulations used a one-phase flow model (as shown above) with a modern minimum-dissipation turbulence LES model (Van der Heiden et al. 2015). Central spatial discretization with Adams-Bashforth time stepping is used throughout. The numerical simulations will be shown for two different, stretched grids: $180 \times 40 \times 60 = 430k$ and $360 \times 80 \times 120 = 3.5M$ grid cells. The grid sizes near the semi-submersible are about 80 cm and 40 cm, respectively, in all three directions. An absorbing boundary condition is applied at the outflow boundary and the simulations are carried out for several wave periods (5-10 periods, depending upon the size of the computational grid). Also results for a locally-refined grid are shown, with cells of around 10 m away from the structure and four refinement levels, down to 50 cm near the object, making a total of 0.5M cells (Fig. 11). Hence this grid is the coarsest in the far field, yet almost the finest in the near field.

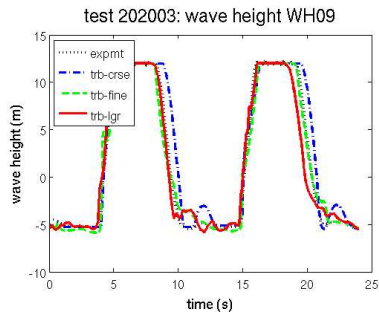


Fig. 12 The wave height development at the first column (WH09) for several grids compared with experimental data.

In the presentation of results we will focus on the region in front of the first column, i.e. monitor points WH09, P11 and P15; see Fig. 10. Firstly, in Fig. 12 the wave run-up against the column is shown for the first two wave periods in the simulation. The results from the locally-refined simulation are pretty similar to those of the finest grid, although the amount of grid points is about 7× less. It is emphasized that this example is mostly momentum driven; only in the run-up phase viscous effects are playing a role.

The pressure development near the bottom (P11) and the top (P15) of the first column of the semi-submersible is shown in Fig. 13. Near the

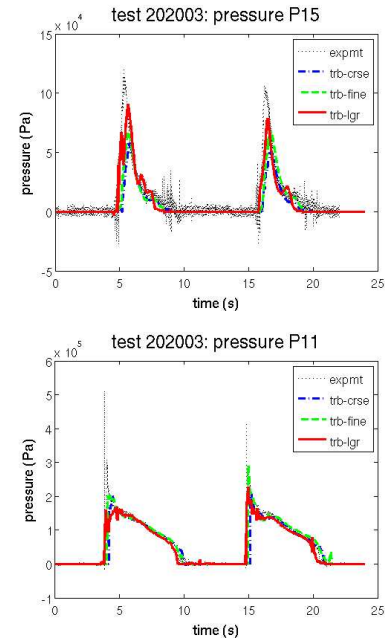


Fig. 13 The pressure at the first column (top P15; bottom P11) for several grids compared with experimental data.

top of the first column, at transducer P15, the peak pressure values in the simulations are relatively low. This can be attributed to the limited number of grid cells along the column causing the run-up process to be badly resolved. A finer grid spacing will likely improve the results in P15 to the quality in P11 at the bottom of the column. More detailed simulations can be found in Wemmenhove (2008, 2015), Van der Plas et al. (2015) and the forthcoming PhD thesis of Van der Plas (2016).

CONCLUSIONS

An overview has been presented of some recent developments in the ComFLOW method designed to simulate and study extreme waves and their impact on falling, floating and moored structures. First a new type of absorbing boundary condition has been presented, which adapts itself to the (local) wave number and phase speed of dispersive waves. An example with an oscillating buoy shows that the computational boundaries can be put close to the wave-generating object. A second example shows a life boat falling into an extreme wave. Here, the interaction between the life boat dynamics and the fluid dynamics of the wave poses serious numerical challenges for their numerical coupling. It is demonstrated that a quasi-simultaneous coupling strategy can efficiently handle these challenges. Finally, large turbulent waves have been ‘attacking’ a fixed semi-submersible, both in simulations as in experiments. In all three examples, local grid refinement has been used to decrease the computational effort without influencing the simulation results too much.

ACKNOWLEDGMENTS

The research is supported by the Dutch Technology Foundation STW, applied science division of NWO and the technology programma of the Ministry of Economic Affairs in The Netherlands (contracts 10475 and 13267).

REFERENCES

Appelö D (2003). *Non-reflecting boundary conditions for wave propagation problems*. PhD thesis, Royal Institute of Technology, Sweden.

- Bayati I, Jonkman J, Robertson A and Platt A (2015). The effects of second-order hydrodynamics on a semisubmersible floating offshore wind turbine. *J Phys: Conf Ser*, Vol 524, 012094.
- Botta EFF and Ellenbroek M (1985). A modified sor method for the poisson equation in unsteady free-surface flow calculations. *J Comput Phys*, Vol 60 (1), pp 119–134.
- Düz B (2015) *Wave generation, propagation and absorption in CFD simulations of free surface flows*. PhD thesis, Technical University Delft.
- Düz B, Borsboom MJA, Veldman AEP, Wellens PR and Huijsmans RHM (2016a). The effect of different volume-of-fluid (VOF) methods on energy dissipation in simulations of propagating water waves. In preparation.
- Düz B, Borsboom MJA, Wellens PR, Veldman AEP and Huijsmans RHM (2016b). An absorbing boundary condition for free-surface water waves. In preparation.
- Düz B, Huijsmans RHM, Veldman AEP, Borsboom M and Wellens P (2013). An absorbing boundary condition for regular and irregular wave simulations. In: L Eça, E Oñate, J Garçia-Espinosa, T Kvamsdal and P Bergan (Eds.), *Computational Methods in Applied Sciences*, Vol 29, Springer.
- Engquist B and Majda A (1977). Absorbing boundary conditions for the numerical simulation of waves. *Math Comput*, Vol 31, pp 629–651.
- Givoli D (1991). Non-reflecting boundary conditions. *J Comput Phys*, Vol 94, pp 1–29.
- Givoli D (2004). High-order local non-reflecting boundary conditions: a review. *Wave Motion*, Vol 39, pp 319–326.
- Hagstrom T (1999). Radiation boundary conditions for the numerical simulation of waves. *Acta Numer*, Vol 8, pp 47–106.
- Higdon R (1986). Absorbing boundary conditions for difference approximations to the multi-dimensional wave equation. *Math Comput*, Vol 47, pp 437–459.
- Higdon R (1987). Numerical absorbing boundary conditions for the wave equation. *Math Comput*, Vol 49, pp 65–90.
- Hirt CR and Nichols BD (1981). Volume of fluid (VOF) method for the dynamics of free boundaries. *J Comput Phys*, Vol 39, pp 201–225.
- Iwanowski B, Lefranc M and Wemmenhove R (2009). CFD simulation of wave run-up on a semi-submersible and comparison with experiment. *Proc 28th Conf Ocean, Offshore and Arctic Engng OMAE2009*, Honolulu (USA), 31 May–5 June, 2009, paper OMAE2009-79052.
- Johannessen TB, Haver S, Bunnik T and Buchner B (2006). Extreme wave effects on deep water TLP's - Lessons learned from the Snorre A model tests. *Proc. Deep Offshore Technology 2006*, Houston, 28–30 November, 2006.
- Kim CH, Clement AH and Tanizawa K (1999) Recent research and development of numerical wave tanks - a review. *Int J Offsh Pol Eng*, Vol 9, ISOPE-99-09-4-241.
- Kleefsman KMT, Fekken G, Veldman AEP, Iwanowski B and Buchner B (2005). A Volume-of-Fluid based simulation method for wave impact problems. *J Comput Phys*, Vol 206, pp 363–393.
- Koo W and Kim MH (2004). Freely floating-body simulation by a 2D fully nonlinear numerical wave tank. *Ocean Eng*, Vol 31, pp 2011–2046.
- Sommerfeld A (1949). *Partial differential equations in physics*. Academic Press.
- Tran TT and Kim D-H (2015). The coupled dynamic response computation for a semi-submersible platform of floating offshore wind turbine. *J Wind Eng Ind Aerodyn*, Vol 147, pp 104–119.
- Tregde V and Nestegard A (2013). Statistical methods for prediction of characteristic loads for free fall lifeboats based on CFD screening results. *Proc. 32nd Int Conf Ocean, Offshore and Arctic Engng OMAE2013*, Nantes (France), 9–14 June, 2013, paper OMAE2013-10296.
- Tsynkov S (1998). Numerical solution of problems on unbounded domains - a review. *Appl Numer Math*, Vol 27, pp 465–532.
- Van der Heiden HJL, Veldman AEP, Luppés R, van der Plas P, Helder J and Bunnik T (2015). Turbulence modeling for free-surface flow simulations in offshore applications. *Proc 34th Int Conf Ocean, Offshore and Arctic Engng OMAE2015*, St. John's (Canada), 31 May–5 June 2015, paper OMAE2015-41078.
- Van der Plas P (2016). *Local grid refinement for free-surface flow simulations*. PhD thesis, University of Groningen.
- Van der Plas P, Veldman AEP, van der Heiden HJL and Luppés R (2015). Adaptive grid refinement for free-surface flow simulations in offshore applications. *Proc 34th Int Conf Ocean, Offshore and Arctic Engng OMAE2015*, St. John's (Canada), 31 May–5 June 2015, paper OMAE2015-42029.
- Veldman AEP (1981). New quasi-simultaneous method to calculate interacting boundary layers. *AIAA J*, Vol 19, pp 79–85.
- Veldman AEP (2001). Matched asymptotic expansions and the numerical treatment of viscous-inviscid interaction. *J Eng Math*, Vol 39, pp 189–206.
- Veldman AEP (2009). A simple interaction law for viscous-inviscid interaction. *J Eng Math*, Vol 65, pp 367–383 (doi: 10.1007/s10665-009-9320-0).
- Veldman AEP, Luppés R, Bunnik T, Huijsmans RHM, Düz B, Iwanowski B, Wemmenhove R, Borsboom MJA, Wellens PR, van der Heiden HJL and van der Plas P (2011). Extreme wave impact on offshore platforms and coastal constructions. *Proc 30th Conf Ocean, Offshore and Arctic Engng OMAE2011*, Rotterdam (The Netherlands), 19–24 June 2011, paper OMAE2011-49488.
- Veldman AEP, Luppés R, van der Plas P, van der Heiden HJL, Helder J and Bunnik T (2015). Turbulence modeling for locally-refined free-surface flow simulations in offshore applications. *Proc Int Symp Offshore and Polar Eng ISOPE2015*, 23–27 June 2015, Kona (Hawaii), paper 2015-TPC-0282.
- Verstappen RWCP (2011). When does eddy viscosity damp subfilter scales sufficiently? *J Scient Comput*, Vol 49, pp 94–110.
- Verstappen RWCP and Veldman AEP (2003). Symmetry-preserving discretization of turbulent flow. *J Comput Phys*, Vol 187, pp 343–368.
- Wellens P (2012). *Wave simulation in truncated domains for offshore applications*. PhD thesis, Delft University of Technology.
- Wemmenhove R (2008). *Numerical simulation of two-phase flow in offshore environments*. PhD thesis, University of Groningen.
- Wemmenhove R, Luppés R, Veldman AEP and Bunnik T (2015). Numerical simulation of hydrodynamic wave loading by a compressible two-phase flow method. *Comp Fluids*, Vol 114, pp 218–231 (doi: 10.1016/j.compfluid.2015.03.007).